Composite Structures 273 (2021) 114302

Contents lists available at ScienceDirect

Composite Structures

journal homepage: www.elsevier.com/locate/compstruct

Effective elastic properties of biocomposites using 3D computational homogenization and X-ray microcomputed tomography

Alp Karakoç [a,b,*], Arttu Miettinen [c], Jussi Virkajärvi [c], Roberts Joffe [d]

[a] Department of Communications and Networking, Aalto University, Finland
[b] Department of Bioproducts and Biotechnology, Aalto University, Finland
[c] Department of Physics, University of Jyväskylä, Jyväskylä, Finland
[d] Department of Engineering Sciences and Mathematics, Luleå University of Technology, Sweden

ARTICLE INFO

Keywords:
Computational homogenization
Biocomposites
Fiber
X-ray microcomputed tomography
Reconstruction

ABSTRACT

A 3D computational homogenization method based on X-ray microcomputed tomography (μCT) was proposed and implemented to investigate how the fiber weight fraction, orthotropy and orientation distribution affect the effective elastic properties of regenerated cellulose fiber-polylactic acid (PLA) biocomposites. Three-dimensional microstructures reconstructed by means of the X-ray μCT were used as the representative volume elements (RVEs) and incorporated into the finite element solver within the computational homogenization framework. The present method used Euclidean bipartite matching technique so as to eliminate the generation of artificial periodic boundaries and use the in-situ solution domains. In addition, a reconstruction algorithm enabled finding the volume and surface descriptions for each individual fiber in a semi-automatic manner, aiming at reducing the time and labor required for fiber labeling. A case study was presented, through which the method was compared and validated with the experimental investigations. The present study is thus believed to give a precise picture of microstructural heterogeneities for biocomposites of complex fiber networks and to provide an insight into the influences of the individual fibers and their networks on the effective elastic properties.

1. Introduction

Recent developments in high-resolution 3D imaging techniques, such as scanning electron microscopy, X-ray computed tomography, and magnetic resonance imaging, have enabled generation of solution domains for numerical analyses from true, physical microstructures [1–5]. This has led to quantification of the mechanical characteristics of a wide variety of materials [6–11]. With the increasing expertise, advances in the image processing and computational methods, and accessibility to the instrumentation, these methods are becoming main-stream tools for development and applications of the predictive numerical models for real-world scenarios [12–14]. Though these methods are very promising in terms of high-fidelity materials characterization, they usually require labor intensive work or advanced-yet-costly algorithm development for generating the solution domain from the image [15]. Especially, for heterogeneous and complex material systems such as textiles, paper and packaging products, nonwoven fabrics and filter mats, nanocellulose substrates and lignocellulosic composites, for which the fiber networks are the reinforcing phase, this process has been widely investigated to provide accurate results in various length scales. It is without doubt that the accurate characterization of fibers and their interactions with the adjacent phases can be directly used to link the microscale and macroscale properties; thus enabling determination of the in-situ effective stiffness and strength properties [16].

In addition to the increasing computational and algorithmic capabilities, the imaging techniques have also matured—e.g. X-ray computed tomography devices capable of nanometer resolution range are nowadays available [17,18], and samples in the cm-scale can be imaged with μm-scale resolution [19]. In order to benefit most from the captured data at nano- and micrometer levels, researchers have been investigating the integration possibilities of multiscale modelling approaches, such as computational homogenization, into 3D imaging techniques [20–22]. Typically, in these scenarios the solution domain is generated from a true microstructure, and therefore some standard assumptions cannot be made. For example, periodic boundary conditions are not applicable as the representative volume elements are not periodic by nature.

* Corresponding author at: Department of Communications and Networking, Aalto University, Finland
E-mail address: alp.karakoc@alumni.aalto.fi (A. Karakoç).

https://doi.org/10.1016/j.compstruct.2021.114302
Received 18 January 2021; Revised 20 May 2021; Accepted 27 June 2021
Available online 1 July 2021

Often, creation of a solution domain from a 3D image of a fibrous material requires separation of the individual fibers from each other, and indeed, there has been various studies focusing on the image acquisition, tracking and characterization of fibers and their interactions. For instance, Aronsson implemented an automatic detection method for hollow objects, which was successfully implemented to combine multiple 2D image slices for paper fiber reconstruction [23]. Bache-Wiig and Henden refined and proposed a similar approach to be used for both paper and fiber-reinforced composite materials [24]. Axelsson and Viguié have presented novel individual fiber tracking methods, taking advantage of the local orientation of the fibers, and obtained good results even for irregularly shaped cellulose fibers [25,26]. In addition to these advancements, a framework to generate 3D microstructure of paper sheet by means of automated image acquisition and probabilistic tracking method was proposed by Donoser, et al. [27]. Recently, Sharma, et al. and Golkhosh, et. al. developed novel algorithms to isolate paper fibers in X-ray microcomputed tomography (μCT) to obtain the in-situ mechanical properties of paper handsheets [16,28], and Malmberg et al. approached the problem of fiber segmentation by finding the contacts between the fibers [29]. Despite the large number of studies done on the topic, an industry-standard method for automatic fiber tracking, able to deal with tightly packed and irregularly shaped fibers, does not seem to be established.

As a contribution to these recent activities, we introduce a framework comprising microstructure generation algorithm with feature labeling through 3-D X-ray μCT imaging and computational homogenization method to characterize the fiber reinforced biodegradable polymer composites, namely biocomposites. The effective elastic properties of these composites were obtained with the schematized workflow in Fig. 1 and compared with the previously carried out experiments by the authors [30]. By means of the framework, morphological description of fibers at microscopic level and the effects of their weight fractions, orthotropy and orientation distributions on the effective elastic properties were analyzed.

2. Methodology

2.1. Microcomputed tomography (μCT) and microstructure generation with feature labeling

Previously it has been shown that X-ray μCT can be efficiently used for generation of solution domain for—e.g. flow simulations [31]. In this image-based modelling approach, a common task is transforming the gray-scale volume image, consisting of pixels, into a representation suitable for the numerical simulation. In finite element-type methods like the one used here, a suitable representation is often a mesh consisting of vertices and tetrahedral elements.

Application of the homogenization framework (described below) requires that each separate material region—i.e. each individual fiber and the matrix—is treated as a separate domain. This description thus provides detailed information of the deformation and damage at fiber, matrix, fiber–matrix interface and fibre–fibre interface levels. For a composite material, this leads to the requirement that each individual reinforcing fiber must be a separate region in the mesh, even if the fibers are in contact with each other. Typically, in a μCT image the fibers are shown as fused isointensity objects and must therefore be separated from each other before or after meshing. We have chosen to separate the individual fibers from each other before generating a mesh.

In order to make an individual fiber segmentation from a binary CT image, where the fiber phase is foreground, we proceed with the method introduced in [32]. This simple method is suitable for solid fibers without a lumen and with a well-defined, preferably circular, cross-section, and it is based on separating fused fibers by morphological operations, followed by labeling of the separated regions. To this end, we use minimum filtering with a spherical structuring element to thin all the fibers such that they separate from each other, as shown in Fig. 2 (a) and (b). After minimum filtering, the remaining regions are labeled such that each region has different label value (please, see Fig. 2 (c)). The labeled regions are then expanded back to the shape of the original structure by morphological reconstruction (please, see Fig. 2 (d)). In addition to separating fibers from each other, this process often breaks single fibers into one large and multiple smaller components—i.e. over-segmentation. Therefore, all components whose volume is less than a selected threshold value are removed and the regions they occupied are re-filled with another application of morphological reconstruction. Finally, the resulting segmentation is checked manually and any badly segmented locations are corrected.

The segmentation process proposed above has two free parameters: the radius of the structuring element used for separation of fused fibers, and the volume threshold used while mitigating over-segmentation. The radius of the structuring element must be smaller than the radius of a fiber as otherwise the minimum filtering process will remove the fiber altogether. On the other hand, the radius must be larger than the radius of any throat between fused fibers (please, see Fig. 2 (a)), as otherwise the fused fibers will not be separated from each other. Typically, the radius is chosen to be approximately one half of the fiber radius. If the fiber radius is not constant, the structuring element radius can be varied accordingly using, e.g., algorithm described in [33].

The threshold volume must be selected to have a value larger than the volume of the small, spurious components created during the minimum filtering and labeling processes, but below the volume of any individual fiber. As the range of suitable threshold values is typically large, the segmentation result is not very sensitive to the particular volume threshold value chosen.

After individual fiber segmentation we apply the CGAL library through the Iso2mesh package to generate a tetrahedral mesh of each fiber and matrix region [34]. The resulting mesh often contains a few badly shaped elements (e.g. very thin) that hinder finite-element simulations. To remove those, we select the vertices that belong to the 5 worst elements by Joe-Liu quality metric [35], and maximize the mesh quality of these elements and their neighbors by moving the selected vertices using the Nelder-Mead optimization algorithm [36]. After optimization, we repeat the process again and iterate until mesh quality is sufficient or does not improve anymore. This iterative process is relatively fast as it is performed only on a small subset of elements, but increases mesh quality significantly. The changes made to the mesh in the optimization phase are very small and do not seem to introduce any significant deviations from the original geometry.

2.2. Three-dimensional computational homogenization

Computational homogenization has been an important tool for in-depth study of material systems with multiple phases and structural hierarchies [37]. Various computational homogenization frameworks have been introduced in the literature, where different length scales have been studied based on the material type—e.g. micro-, meso-, and macroscales for composite laminates; and micro- and macroscales in short fiber reinforced composites, as is the case in this paper [38]. The coupling between these scales and their relation with the macroscale deformations provide optimized design and manufacturing processes, which principally reduces labor-intense mechanical testing procedures and costs. In this context, for the present study on the biocomposites, a micro–macro length scale coupling was used, for which the microscale refers to the specimen microstructure and macroscale refers to the tested specimen itself.

The present computational homogenization framework is an upscaling technique based on the coupling of different length scales, for which the information is passed from finer length scales to coarser

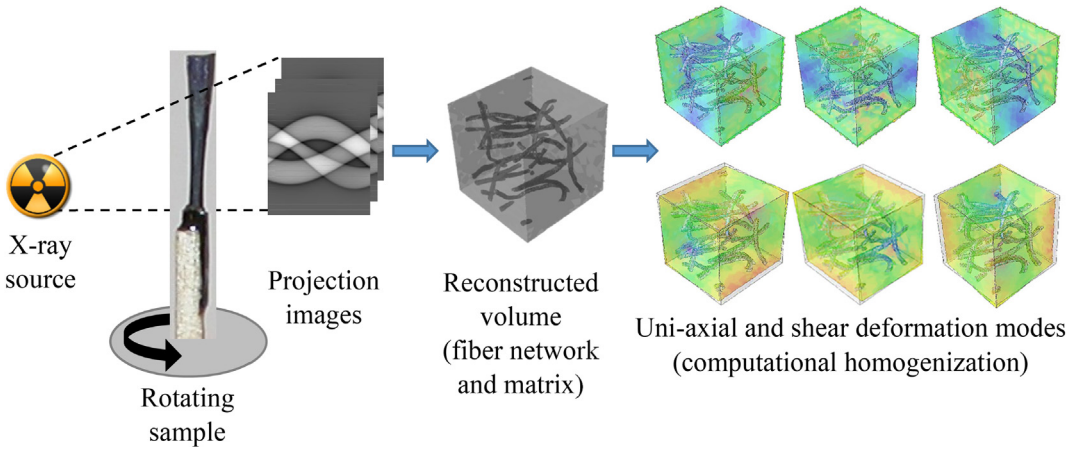

Fig. 1. The present framework comprising X-ray computed tomography and computational homogenization methods.

Fig. 2. Schematic of the individual fiber segmentation process. (a) Original image showing two fused fiber cross-sections (top left) and one individual fiber cross-section (bottom right), where the red line shows the diameter of a throat between the fused fibers, (b) minimum filtering with a spherical structuring element results in fused fibers being separated from each other, (c) the separated regions are labeled, and (d) extruded back to the original shape by morphological reconstruction. (For interpretation of the references to color in this figure legend, the reader is referred to the web version of this article.)

scales (not vice versa) by solving the boundary value problem (BVP) on the representative volume element (RVE). By means of the averaging theorems—e.g. Hill-Mandel (or macro-homogeneity) condition, or parametric identification—simulations at the microscale are used to determine the effective properties at the macro-scale describing the continuum behavior [39].

As illustrated in Fig. 3, the framework uses Euclidean bipartite matching[1] for defining the periodic boundary condition and solve the BVP in the case that geometrical periodicity condition is not possible to obtain over the volume of reconstructed domains. Domains of this type are generated with stochastic modelling or image reconstruction methods e.g. from tomographic images [40,41] and result in non-conformal meshes with the non-matching boundary node distributions. The framework uses a control node set q that is kinematically coupled with the boundary node set p of the RVE boundary domain $\partial\omega$. The total distance between p and q sets is minimized through Euclidean bipartite matching in order to determine the nearest nodes among the sets. The $n \times n$ distance matrix

$$\begin{bmatrix} \mathbf{d}(p_1,q_1) & \mathbf{d}(p_1,q_2) & \dots & \mathbf{d}(p_1,q_n) \\ \mathbf{d}(p_2,q_1) & \dots & \dots & \dots \\ \dots & \dots & \dots & \dots \\ \mathbf{d}(p_n,q_1) & \dots & \dots & \mathbf{d}(p_n,q_n) \end{bmatrix} \tag{1}$$

is generated based on the Euclidean distance $\mathbf{d}$ of each (p, q) combination with n being the set length of p and q. The optimal permutation for the matching nodes is obtained as the minimizer of

$$T = \sum_{\prod} \mathbf{d}(p,q) \tag{2}$$

where T is the total Euclidean distance and $\prod$ is a set of (p, q) pairs abiding a one-to-one correspondence between the two node sets [42,43]. The matching nodes are then kinematically coupled. The boundary conditions are defined on the control domain $\partial\Gamma$ comprised of q. BVP is then solved—e.g. via strain driven homogenization—for which the macro-scale strain $\mathbf{e}^{\mathrm{M}}$ is used as the driving parameter of the microscopic displacement field such that

$$\overrightarrow{u}^{\mathrm{m}} = \overrightarrow{r} \cdot \mathbf{e}^{\mathrm{M}} + \underrightarrow{u}. \tag{3}$$

here, $\overrightarrow{r}$ is the position vector between two nodes; thus, $\overrightarrow{r} \cdot \mathbf{e}^{\mathrm{M}}$ refers to the macroscopic displacement contribution and $\underrightarrow{u}$ is displacement fluctuations arising from heterogeneities. Continuity conditions for the displacement field are then satisfied at $\partial\Gamma$ by applying Equation to the control node sets q, which eliminates $\underrightarrow{u}$. By implementing the Hill-Mandel (or macro-homogeneity) condition, coupling between the micro- and macroscales is formed. Eventually, macro-scale stress $\mathbf{s}^{\mathrm{M}}$ is computed as the volume average of the microscale stress $\mathbf{s}^{\mathrm{m}}$ as follows

$$\mathbf{s}^{\mathrm{M}} = \frac{1}{\Gamma} \int_{\Gamma} \mathbf{s}^{\mathrm{m}} \, \mathrm{d}\Gamma. \tag{4}$$

The given $\mathbf{e}^{\mathrm{M}}$ and the computed $\mathbf{s}^{\mathrm{M}}$ can be combined to determine the compliance $\mathbf{C}^{\mathrm{M}}$—here, with the least-squares minimization of six distinct deformation modes in three-dimensional space (three axial tension $\mathbf{e}^{\mathrm{M}}_{XX}$, $\mathbf{e}^{\mathrm{M}}_{YY}$, $\mathbf{e}^{\mathrm{M}}_{ZZ}$ and three shear $\mathbf{e}^{\mathrm{M}}_{XY}$, $\mathbf{e}^{\mathrm{M}}_{YZ}$, $\mathbf{e}^{\mathrm{M}}_{ZX}$ loading modes) as

$$C(C_{11},..,C_{66}) = \sum_{i=1}^{n} \| \mathbf{e}^{\mathrm{M}}_i - \mathbf{C}^{\mathrm{M}} : \mathbf{s}^{\mathrm{M}}_i \|^2. \tag{5}$$

Here, i refers to the number of experiments. Under the assumptions of small strains and orthotropic material, $\mathbf{C}^{\mathrm{M}}$ can be expressed as

[1] Available at https://github.com/metudust/Euclidean-Bipartite-Matching/.

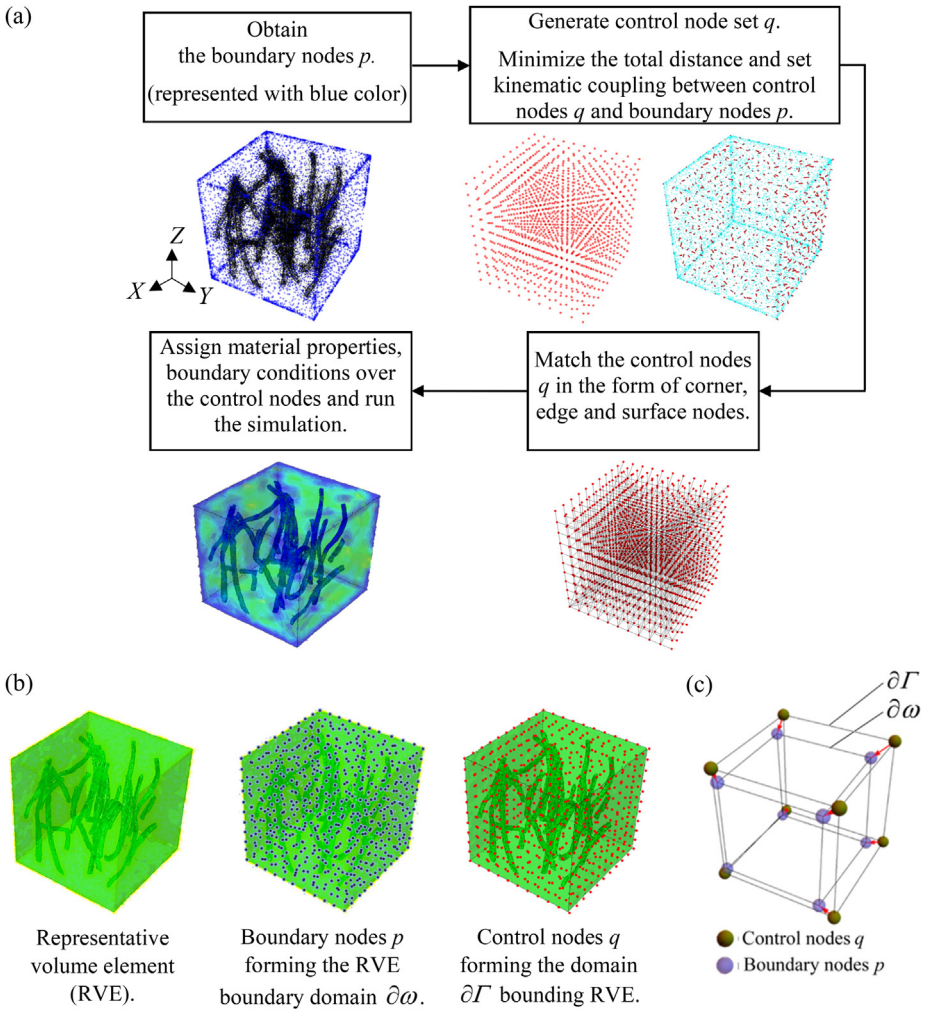

Fig. 3. Computational homogenization of three-dimensional fibrous materials: (a) the workflow, (b) representative volume element (RVE) boundary domain represented with $\partial\omega$, domain $\partial\Gamma$ bounding RVE, boundary nodes p on $\partial\omega$ and control nodes q comprising of vertices, edge and surface nodes on $\partial\Gamma$, (c) bipartite matching between control and boundary nodes.

$$[\mathbf{C}^{\mathrm{M}}] = \begin{bmatrix} 1/E_X & -\nu_{YX}/E_Y & -\nu_{ZX}/E_Z & 0 & 0 & 0 \\ -\nu_{XY}/E_X & 1/E_Y & -\nu_{ZY}/E_Z & 0 & 0 & 0 \\ -\nu_{XZ}/E_X & -\nu_{YZ}/E_Y & 1/E_Z & 0 & 0 & 0 \\ 0 & 0 & 0 & 1/G_{YZ} & 0 & 0 \\ 0 & 0 & 0 & 0 & 1/G_{ZX} & 0 \\ 0 & 0 & 0 & 0 & 0 & 1/G_{XY} \end{bmatrix} \tag{6}$$

for which E_X, E_Y, E_Z are the elastic moduli, G_{YZ}, G_{ZX}, G_{XY} are the shear moduli and $\nu_{XY}, \nu_{YX}, \nu_{XZ}, \nu_{ZX}, \nu_{YZ}, \nu_{ZY}$ are the Poisson's ratios defined in the global (specimen) *XYZ*-Cartesian coordinate system as depicted in Fig. 3.

3. Results and discussions

3.1. Mechanical properties by tensile testing

In order to test the present FEM framework, PLA composites reinforced with regenerated cellulose fibers were manufactured. Reinforcement was CORDENKA® 700 Super 3 regenerated cellulose fibers with the density of $\rho_{\mathrm{f}} = 2440$ kg/m^3 (by CORDENKA GmbH, Germany) [44]. Fiber were supplied as twisted continuous bundles (100 twists per meter) containing 1350 individual filaments with a diameter of 12.5 μm. As the matrix, PLA Ingeo biopolymer 2003D with $\rho_{\mathrm{m}} = 1240$ kg/m^3 supplied in the form of pellets by NatureWorks LLC (USA) was used [45]. The 2 mm long fibers were obtained by manually chopping continuous CORDENKA fibers using in-house made cutting device consisting of 60 razor blades. The chopped fibers and PLA pellets were mixed and homogenized in a twin-screw Brabender PLE 650 at 215^{0}C (to achieve melting of PLA). The content of fibers in composite pellets was chosen according to the desired nominal fiber weight fractions of 5%, 10% and 15%. The hot compound was removed from the mixer and immediately transferred to the hot press pre-heated to 80^{0}C in order to make 2 mm thick plate. This plate was cooled to the room temperature and cut into small pieces (square pellets with approximate edge length of 3–5 mm). The composite pellets were fed into HAAKE™ MiniJet laboratory injection molding machine to manufacture tensile specimens according to the ASTM D638 standard (dimensions according to type 5 specimen in the standard) [46].

Table 1
Tensile properties of the investigated composites. Here, the loading direction was aligned with the *Z*-axis of the specimens (please, see Fig. 3(a)).

Fiber weight fraction (%)	E ($\approx E_Z$) (GPa)	σ_{UTS} (MPa)	$\varepsilon_{\mathrm{fail}}$ (%)
5	3.36 ± 0.21	59.19 ± 0.20	22.92 ± 3.19
10	3.72 ± 0.19	65.81 ± 0.25	9.24 ± 0.58
15	4.55 ± 0.13	70.78 ± 1.54	7.58 ± 0.98

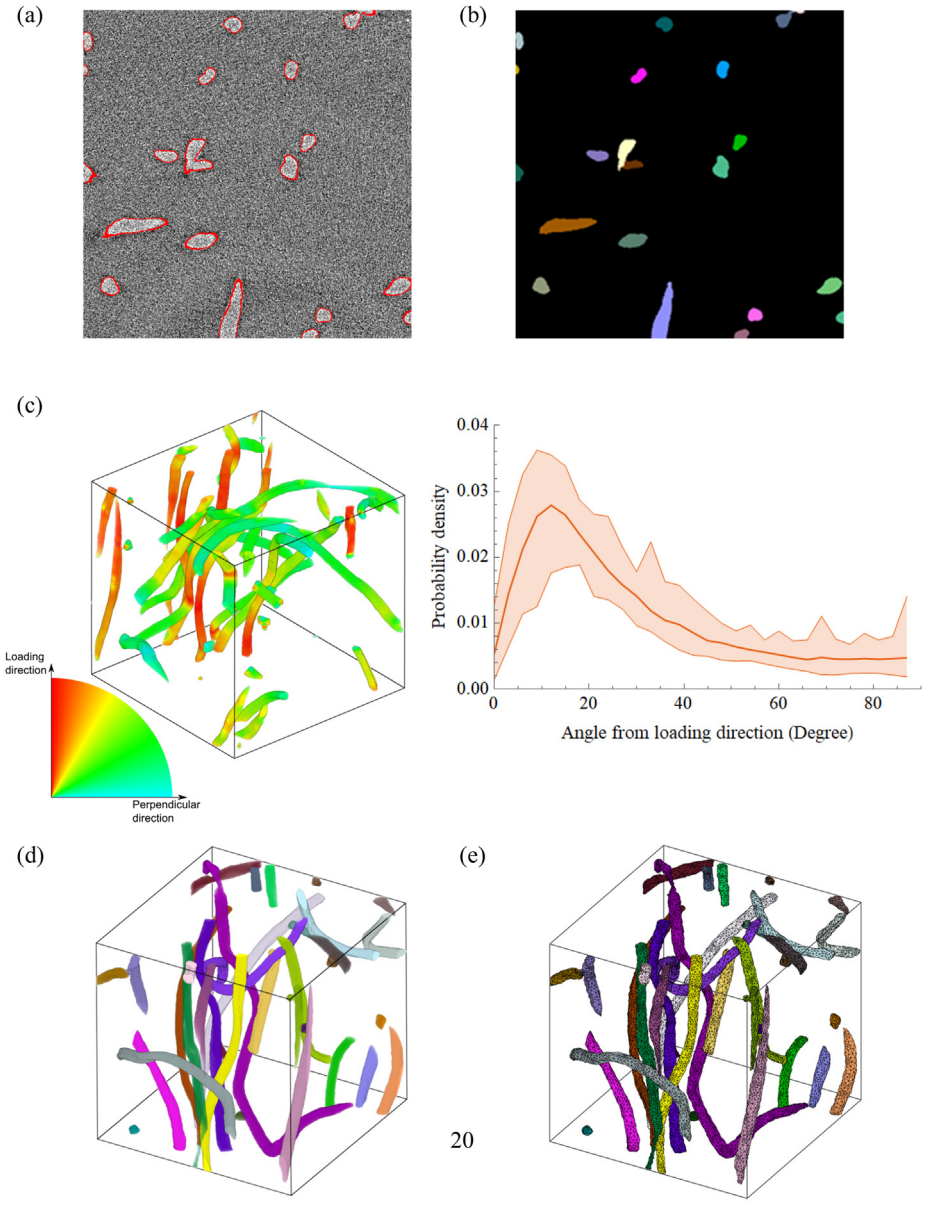

Fig. 4. (a) Slice through the original CT image with red lines denoting the borders between the foreground and the background in the corresponding binary image. (b) The same slice than in (a) after individual fiber segmentation. Each individual fiber has been colored with random color. (c) 3D visualization of the fiber orientation determined with the structure tensor method for an RVE and probability distribution band of the fiber orientations for the investigated RVEs (based on the local minima and maxima). (d) 3D visualization of the segmented fiber phase after individual fiber segmentation, and (e) 3D visualization of the fiber phase of the mesh. In all the panels, width, height, and depth of the visible region is 265 μm. (For interpretation of the references to color in this figure legend, the reader is referred to the web version of this article.)

Tensile tests were then carried out at ambient conditions on the lab (temperature of 23.5^{o}C and relative humidity of 42%) on Instron 3366 machine equipped with 10kN load cell and extensometer with 12.5 mm gauge length. The tests were conducted in displacement-controlled mode with the cross-head separation speed corresponding to the loading rate of 1%/min. Specimens were loaded until the failure while the load and strain were registered during the tests, the elastic modulus E ($\approx E_z$), ultimate tensile strength (σ_{UTS}) and strain at failure ($\varepsilon_{\mathrm{fail}}$) of which are listed in Table 1. In each batch, the tested composites contained up to five specimens in order to obtain reliable statistics.

3.2. Microcomputed (μCT) tomography and mesh generation

Samples for μCT were taken from the central part of the tensile test specimens manufactured with the desired and abovementioned fiber weight fractions of 5%, 10% and 15%, respectively. Cylinders of approximately 1 mm diameter were extracted from each specimen using a rotary tool. The cylinders were mounted on top of a carbon fiber rod.

Microtomographic images of the samples were acquired using Xradia microCT-400 device with 0.59 μm pixel size. Acceleration voltage and power of the X-ray tube were set to 30 kV and 3.5 W, respectively. Total of 2025 projection images with 23 s exposure time for each of them were acquired, resulting in 15 h total imaging time per sample. The projections were reconstructed using the filtered back-projection algorithm.

The reconstructions were filtered with Gaussian high-pass filter to remove any global gray-scale variations ($\sigma = 5.9$Aμm), followed by approximate bilateral filtering [47] to remove imaging noise (spatial $\sigma = 1.77$Aμm, radiometric $\sigma \approx 20\%$ of full value range). The filtered

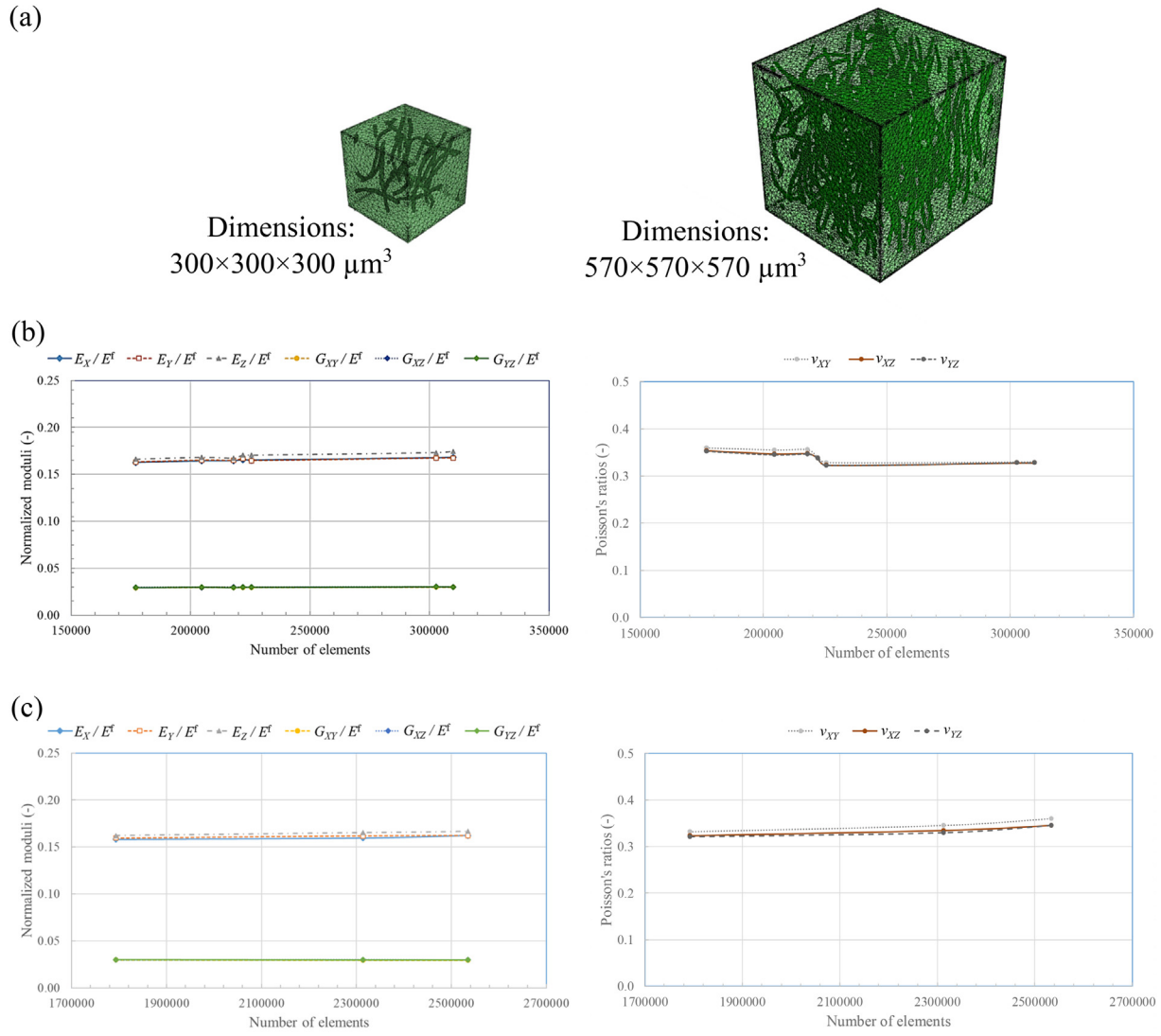

Fig. 5. RVE size: (a) exemplary small (left, 300 × 300 × 300 μm^3 and fiber weight fraction of 6.14%) and large (right, 570 × 570 × 570 μm^3 and fiber weight fraction of 6.65%) solution domains. Number of elements and effective elastic properties for (b) small and (c) large solution domains. The effective elastic and shear moduli are shown normalized with the fiber elastic modulus $E^f = 19.52$ GPa.

images were thresholded using the Otsu method [48]. Remaining small, spurious background and foreground regions, caused by imaging noise remaining after filtering, were eliminated by morphological opening followed by morphological closing with a spherical structuring element ($r = 2.95$Aμm).

RVEs of desired size were cropped from the binary images and meshed according to the procedure described above in the Section 2.1. The cross-sections of the fibers were slightly oval, with diameter between 6 μm and 18 μm. The radius of the spherical structuring element used for separation of fused fibers was set to 3 μm, a value between limits of 1.5 μm and 4.5 μm given by the rule discussed in Section 2.1. The volume threshold used for mitigation of oversegmentation was 600 μm^3. These parameter choices lead to visually correct segmentation, an example of which is shown in Fig. 4.

The fiber orientation distribution of each RVE was determined with the structure tensor method [49]. The structure tensor for a pixel at $\vec{x}$ is defined as

$$S_{ij} = G_{\sigma_t} * \left(\frac{\partial f}{\partial x_i} \frac{\partial f}{\partial x_j} \right) \tag{7}$$

where f is the thresholded binary image, G_{σ_t} is a Gaussian function with standard deviation σ_t, and $*$ denotes convolution. The partial derivatives are approximated using a convolution with another Gaussian function as

$$\frac{\partial f(\vec{x})}{\partial x_i} \approx \left(\frac{\partial G_{\sigma_s}}{\partial x_i} * f \right)(\vec{x}) \tag{8}$$

The local fiber orientation at $\vec{x}$ is given by the eigenvector of $S_{ij}(\vec{x})$ corresponding to the smallest eigenvalue. The angle between the local fiber orientation and the long axis of the dogbone specimen was calculated and binned into an orientation distribution. The smoothing parameters were chosen to be $\sigma_s = \sigma_t = 2.95$Aμm. The image reconstruction and analysis processes were performed using the pi2 software package[2], and 3D visualizations with MeVisLab[3].

[2] Available at https://github.com/arttumiettinen/pi2
[3] Available at https://www.mevislab.de/

Table 2
Computed effective elastic properties of the composites with isotropic fibers.

Fiber weight fraction (%) (nominal)	Fiber weight fraction (%) (measured)	E_X (GPa)	E_Y (GPa)	E_Z (GPa)	G_{XY} (GPa)	G_{XZ} (GPa)	G_{YZ} (GPa)	ν_{XY}	ν_{XZ}	ν_{YZ}
5	4.92	3.17	3.18	3.25	0.57	0.58	0.58	0.36	0.35	0.35
	5.63	3.21	3.22	3.27	0.58	0.58	0.58	0.36	0.35	0.35
	5.70	3.21	3.22	3.28	0.58	0.58	0.58	0.35	0.35	0.34
	5.98	3.22	3.21	3.33	0.58	0.59	0.58	0.33	0.32	0.32
	6.14	3.23	3.26	3.33	0.58	0.58	0.58	0.34	0.34	0.34
	7.12	3.27	3.27	3.38	0.58	0.59	0.59	0.33	0.33	0.33
	7.32	3.28	3.27	3.41	0.59	0.59	0.59	0.33	0.33	0.33
	Mean	3.23	3.23	3.32	0.58	0.58	0.58	0.34	0.34	0.34
	Std. Dev.	0.04	0.03	0.05	0.01	0.01	0.01	0.01	0.01	0.01
	7.07	3.26	3.28	3.39	0.59	0.59	0.60	0.33	0.33	0.33
	7.74	3.28	3.32	3.45	0.59	0.59	0.60	0.34	0.31	0.31
	8.77	3.33	3.33	3.54	0.59	0.60	0.60	0.34	0.32	0.31
	9.22	3.36	3.35	3.54	0.60	0.61	0.60	0.33	0.30	0.30
	9.30	3.35	3.36	3.55	0.60	0.60	0.61	0.32	0.33	0.33
10	9.69	3.38	3.37	3.56	0.60	0.61	0.60	0.32	0.33	0.33
	10.51	3.40	3.39	3.65	0.61	0.61	0.61	0.33	0.33	0.33
	10.65	3.41	3.40	3.66	0.60	0.61	0.61	0.32	0.33	0.33
	Mean	3.36	3.36	3.57	0.60	0.60	0.60	0.33	0.32	0.32
	Std. Dev.	0.04	0.03	0.07	0.01	0.01	0.01	0.01	0.01	0.01
	10.33	3.41	3.42	3.60	0.60	0.60	0.60	0.35	0.35	0.35
	10.40	3.36	3.39	3.62	0.62	0.62	0.62	0.35	0.35	0.35
	11.98	3.48	3.46	3.68	0.62	0.63	0.63	0.33	0.32	0.32
	13.49	3.54	3.52	3.78	0.63	0.64	0.64	0.32	0.31	0.31
15	13.78	3.55	3.55	3.84	0.62	0.64	0.62	0.33	0.33	0.33
	13.86	3.57	3.54	3.85	0.63	0.65	0.63	0.34	0.33	0.34
	14.24	3.58	3.56	3.88	0.63	0.65	0.64	0.34	0.34	0.33
	14.66	3.60	3.58	3.90	0.62	0.62	0.62	0.33	0.33	0.33
	Mean	3.53	3.51	3.79	0.62	0.63	0.63	0.33	0.33	0.33
	Std. Dev.	0.08	0.06	0.10	0.01	0.02	0.01	0.01	0.01	0.01

3.3. Effective elastic properties via the present framework

The present framework was used to understand how the weight fraction, orientation distribution and orthotropy of the fibers influence the effective elastic properties of the regenerated cellulose fiber-PLA biocomposites under the assumption of linear elasticity. Maximum macro-scale strain value of $\max(e_{ij}^{M}) = 0.025$ was used as the input, for which $i,j = \{X, Y, Z\}$. As the first step, the RVE size was determined. Thereafter, the weight fraction and orientation distribution of fibers with isotropic material properties were investigated. The regenerated cellulose fibers were assumed to have the following the literature values $E^{\mathrm{f}} = 19.52$ GPa and $\nu^{\mathrm{f}} = 0.3$ while PLA matrix was assigned to have $E^{\mathrm{m}} = 2.95$ GPaand $\nu^{\mathrm{m}} = 0.36$ [30,44]. In order to define the suitable RVE size, two different volumes—i.e. $300 \times 300 \times 300$ μm^3 and $570 \times 570 \times 570$ μm^3— were analyzed with the closest possible fiber weight fractions obtained from the X-ray μCT imaging. The fiber weight fractions were ~ 6.14% and ~ 6.65%, respectively. This investigation implied that there was a negligible effect of mesh size for the selected range of elements on the normalized effective elastic properties E_X/E_f, E_Y/E_f, E_Z/E_f, G_{XY}/E_f, G_{XZ}/E_f, G_{YZ}/E_f, ν_{XY}, ν_{XZ}, ν_{YZ} with relative differences of 3.2%, 2.6%, 3.1%, 0.3%, 0.1%, 0.2%, 0.8%,0.9% and 1.6% on average, respectively, which are also shown in Fig. 5. Based on these values and plots, the RVE size of $300 \times 300 \times 300$ μm^3 was deduced to suffice and implemented for the investigations.

After determining the suitable RVE size, numerical analyses were carried out with the abovementioned material properties. Through these analyses, the effective elastic properties and their correlations with the fiber weight fractions and orientation distributions were investigated. The nominal and measured (through tomography images) fiber weight fractions, and the corresponding numerical results were listed in Table 2. These results were compared with the previously conducted experiments listed in Table 1 on the basis of the effective elastic modulus E_Z, which resulted in relative errors of 1.2%, 4.2% and 20% for the batches of 5%, 10% and 15% nominal fiber weight fractions, respectively. The main source of error was assumed to be the fact that the RVEs capture partial fiber segments rather than whole fibers (see Fig. 6(a) and 7). For whole fibers to fit in the RVEs, they would need to be very large, leading to a prohibitive number of elements and very long computing times. Such large models were not feasible to solve with the available computational resources.

Based on the listed mean values in Table 2 and the plot depicted in Fig. 6(b), the correlation between the fiber weight fraction and effective elastic properties$E_X, E_Y, E_Z, G_{XY}, G_{XZ}, G_{YZ}$ resulted in an increase of 8.5%, 8.7%, 14.2%, 6.9%, 8.6% and 8.6% in comparison with the minimum nominal (5%) and maximum nominal (15%) fiber weight fractions, respectively. In addition, the close relationship between the fiber orientation distribution and effective elastic moduli, which dictated $E_Z > E_Y \approx E_X$ and was more prominent with the increasing fiber weight fractions, was also deduced based on the quantitative image analysis (please, see Fig. 4(c)) and tabulated numerical results. This relationship was mainly due to the fiber orientation induced by the polymer melt flow during the injection molding process, which results in the increasing probability of fiber alignment along the loading direction aligned with the Z-axis in the present study. Contrarily, the comparison of the Poisson's ratios with respect to the minimum and maximum nominal fiber weight fractions demonstrated slight decreases (-2.9%) as observed in Table 2.

Following the investigations with isotropic fibers, a novel approach for the effect of fiber orthotropy on the effective elastic properties was provided. Since there are very few studies on the orthotropic properties of the regenerated cellulose fibers, the fibers were assumed to have $E_x^{\mathrm{f}} = 19.52$ GPa, $E_y^{\mathrm{f}} = E_z^{\mathrm{f}} = 6.5$ GPa, $G_{xy}^{\mathrm{f}} = G_{xz}^{\mathrm{f}} = 4.5$ GPa, $G_{yz}^{\mathrm{f}} = 1.5$ GPa, $\nu_{xy}^{\mathrm{f}} = \nu_{xz}^{\mathrm{f}} = 0.07$ and $\nu_{yz}^{\mathrm{f}} = 0.39$. These approximate properties were reproduced from the previously conducted fiber characterization studies [50–52]. It is noteworthy that the subscripts $\times$,y

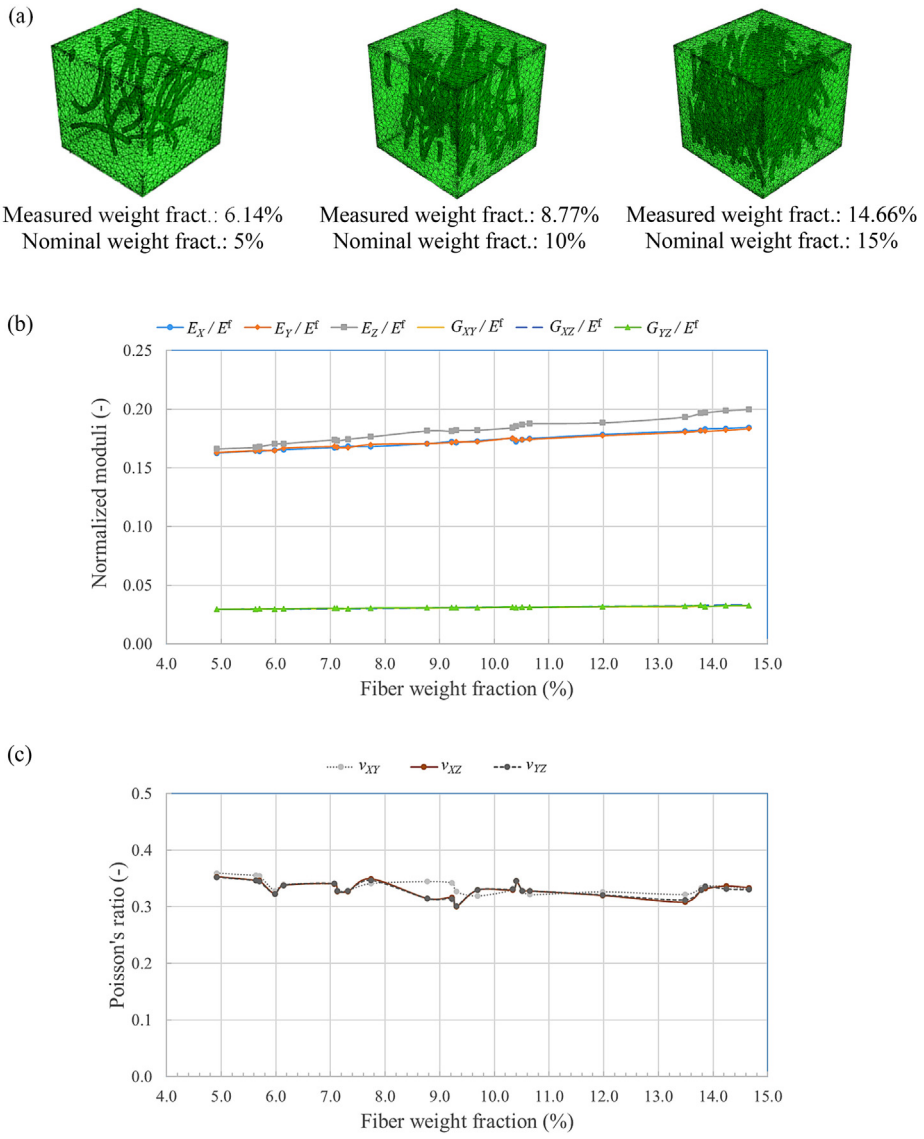

Fig. 6. Effect of fiber weight fractions: (a) representation of RVEs with different fiber weight fractions, (b) fiber weight fractions versus normalized effective elastic properties, for which the fiber elastic modulus $E^f = 19.52$ GPa, (c) fiber weight fraction versus Poisson's ratios.

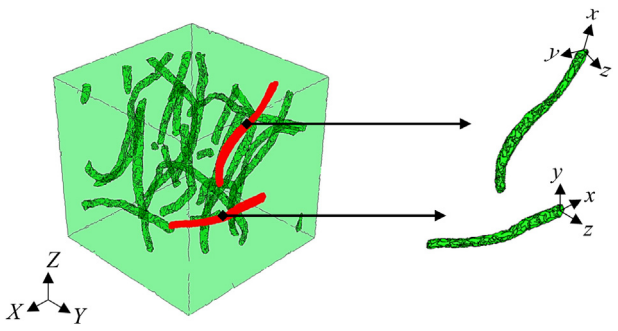

Fig. 7. A representative volume element (RVE) with its global *XYZ*-Cartesian coordinate system (*XYZ*) and the constituent fibers with their local (fiber) *xyz*-Cartesian coordinate systems.

and *z* refer to the axes of the local (fiber) *xyz*-Cartesian coordinate system as illustrated in Fig. 7. These axes were roughly determined through the Karhunen–Loève transform (KLT) (also known as Eigenvector transform), the detailed descriptions for which can be found in the literature [53–55]. A Mathematica notebook for KLT, which includes a fiber node set and the built-in "KarhunenLoeveDecomposition" function, is also available as Supplementary Material. As listed in Table 3, the effective moduli for this study were obtained to be lower than the study on isotropic fibers, which was a natural outcome due to the selected fiber material properties. The results demonstrated increasing trends for E_X, E_Y, E_Z, G_{XY}, G_{XZ}, G_{YZ}, which were 3.9%, 2.9%, 8.6%, 1.8%, 5.4%, 3.5% for the minimum and maximum nominal fiber weight fractions—i.e. 5% and 15%, respectively. Similar to the previous investigations on the isotropic fibers, $E_Z > E_Y \approx E_X$ was observed, which points out the effect of fiber orientation distribution on the effective elastic moduli. On the other hand, 2.6% relative increase for ν_{XY} and −5.5% relative decrease for both ν_{XZ} and ν_{YZ} were obtained with the abovementioned minimum and maximum nominal fiber weight fractions.

4. Conclusions

In the current study, a 3D X-ray μCT based computational homogenization framework was presented to understand the effects of the fiber weight fraction, orientation distribution and orthotropy on the

Table 3
Computed effective elastic properties of the composites with orthotropic fibers.

Fiber weight fraction (%) (nominal)	Fiber weight fraction (%) (measured)	E_X (GPa)	E_Y (GPa)	E_Z (GPa)	G_{XY} (GPa)	G_{XZ} (GPa)	G_{YZ} (GPa)	ν_{XY}	ν_{XZ}	ν_{YZ}
5	4.92	3.07	3.08	3.15	0.55	0.56	0.56	0.38	0.37	0.37
	6.14	3.13	3.17	3.29	0.56	0.57	0.58	0.38	0.36	0.36
	7.12	3.11	3.11	3.30	0.56	0.57	0.57	0.39	0.36	0.36
	Mean	3.11	3.12	3.24	0.56	0.56	0.57	0.38	0.36	0.36
	Std. Dev.	0.03	0.05	0.08	0.01	0.01	0.01	0.01	0.01	0.01
	7.74	3.14	3.13	3.31	0.56	0.57	0.57	0.39	0.36	0.35
	8.77	3.14	3.14	3.38	0.56	0.57	0.57	0.38	0.34	0.34
10	9.69	3.18	3.15	3.38	0.57	0.58	0.58	0.39	0.35	0.35
	Mean	3.15	3.14	3.36	0.56	0.57	0.57	0.39	0.35	0.35
	Std. Dev.	0.02	0.01	0.04	0.01	0.01	0.01	0.01	0.01	0.01
	10.40	3.19	3.17	3.43	0.58	0.57	0.58	0.39	0.37	0.36
	13.49	3.24	3.22	3.51	0.57	0.59	0.59	0.39	0.34	0.34
15	14.66	3.27	3.23	3.62	0.57	0.60	0.59	0.38	0.33	0.33
	Mean	3.23	3.21	3.52	0.57	0.59	0.59	0.39	0.34	0.34
	Std. Dev.	0.04	0.03	0.10	0.01	0.02	0.01	0.01	0.02	0.02

effective elastic properties of regenerated cellulose fiber-PLA biocomposites. X-ray μCT was used to reconstruct the RVEs from the tested specimens with the nominal fiber weight fractions of 5%, 10% and 15% (measured weight fraction range of 4.92%-14.66% through X-ray μCT). Based on the experimental and numerical comparisons for the effective elastic modulus E_Z of the biocomposites, the relative error was obtained to be 1.2%, 4.2% and 20% for the batches of 5%, 10% and 15% nominal fiber weight fractions, respectively. There was an increasing trend of the relative errors with the weight fractions. The relative errors could be minimized with the selection of extremely large RVEs capturing the whole fibers rather than their partial segments, which was experienced here. However, this would lead to drastic increase in the element count and computational costs, which requires rigorous investigations on the code optimization and high-performance computing of tomographic imaging and numerical analyses. Thus, as a future work, feasibility study from the computational point of view will be carried out.

The numerical investigations demonstrated the positive influence of the fiber weight fraction on both the elastic and shear moduli while the change in weight fraction was observed to be less effective for the Poisson's ratios. In addition to these findings, X-ray μCT images also indicated that there was a preferential orientation of fibers. This was verified by quantitative image analysis and the numerical results — i.e. $E_Z > E_Y \approx E_X$. The framework and its outcomes are believed to advance the current state-of-the-art in the biocomposites characterization, which combines the high-fidelity microstructural imaging, reconstruction, 3D image-based computational homogenization and experimental mechanics.

Author contributions

All the authors contributed to the manuscript. AK developed and coded the numerical framework, AM generated and coded the image processing tools and solution domains to be used for the numerical analyses, RJ provided the materials to be used in X-ray μCT and the results of the mechanical tests. JV performed the X-ray μCT experiments and AK carried out the numerical analyses.

CRediT authorship contribution statement

Alp Karakoç: Conceptualization, methodology, software, investigation, writing - review & editing. **Arttu Miettinen:** Conceptualization, methodology, software, investigation, writing - review & editing. **Jussi Virkajärvi:** Methodology, investigation. **Roberts Joffe:** Conceptualization, methodology, writing - review & editing.

Declaration of Competing Interest

The authors declare that they have no known competing financial interests or personal relationships that could have appeared to influence the work reported in this paper.

Acknowledgments

AK gratefully acknowledges the funding through the postdoctoral researcher position at Aalto University Department of Bioproducts and Biosystems, Academy of Finland BESIMAL (Decision No. 334197) and the research fellowship at Aalto University Department of Communications and Networking.

Appendix A. Supplementary data

Supplementary data to this article can be found online at https://doi.org/10.1016/j.compstruct.2021.114302.

References

[1] Madra A, Adrien J, Breitkopf P, Maire E, Trochu F. A clustering method for analysis of morphology of short natural fibers in composites based on X-ray microtomography. Compos Part A Appl Sci Manuf 2017;102:184–95. https://doi.org/10.1016/j.compositesa:2017.07.028.
[2] Bénézech J, Couégnat G. Variational segmentation of textile composite preforms from X-ray computed tomography. Compos Struct 2019;230:111496. https://doi.org/10.1016/j.compstruct.2019.111496.
[3] Huang W, Causse P, Brailovski V, Hu H, Trochu F. Reconstruction of mesostructural material twin models of engineering textiles based on Micro-CT Aided Geometric Modeling. Compos Part A Appl Sci Manuf 2019;124:105481. https://doi.org/10.1016/j.compositesa:2019.105481.
[4] Wintiba B, Vasiukov D, Panier S, Lomov SV, Ehab Moustafa Kamel K, Massart TJ. Automated reconstruction and conformal discretization of 3D woven composite CT scans with local fiber volume fraction control. Compos Struct 2020;248:112438. https://doi.org/10.1016/j.compstruct.2020.112438.
[5] Wang P, Wen J, Lei H, Xu B, Liu Y, Yang Le, et al. Morphology characterization and in-situ three-dimensional strain field monitor of short carbon fiber-reinforced polymer composites under tension. Compos Struct 2021;262:113634. https://doi.org/10.1016/j.compstruct.2021.113634.
[6] Huang W, Xu R, Yang J, Huang Q, Hu H. Data-driven multiscale simulation of FRP based on material twins. Compos Struct 2021;256:113013. https://doi.org/10.1016/j.compstruct.2020.113013.
[7] Duval L, Moreaud M, Couprie C, Jeulin D, Talbot H, Angulo J, et al. Image processing for materials characterization: Issues, challenges and opportunities. In: Conf. Image Process. ICIP; 2014. p. 2014. https://doi.org/10.1109/ICIP.2014.7025985.
[8] Huang X, Wei B. Mineral particle image processing and parameter extracting. In: 2010 Int Conf. Logist. Eng. Intell. Transp. Syst. LEITS2010 - Proc.. https://doi.org/10.1109/LEITS.2010.5664979.
[9] Joffre T, Miettinen A, Berthold F, Gamstedt EK. X-ray micro-computed tomography investigation of fibre length degradation during the processing steps of short-fibre composites. Compos Sci Technol 2014;105:127–33. https://doi.org/10.1016/j.compscitech.2014.10.011.

[10] Miettinen A, Chinga-Carrasco G, Kataja M. Three-dimensional microstructural properties of nanofibrillated cellulose films. Int J Mol Sci 2014;15(4):6423–40. https://doi.org/10.3390/ijms15046423.

[11] Zhang J, Subasinghe N. Extracting ore texture information using image analysis. Trans Institut Min Metall Sect C Miner Process Extr Metall 2012;121(3):123–30. https://doi.org/10.1179/1743285512Y.0000000011.

[12] Taylor CA, Figueroa CA. Patient-specific modeling of cardiovascular mechanics. Annu Rev Biomed Eng 2009;11(1):109–34. https://doi.org/10.1146/annurev.bioeng.10.061807.160521.

[13] Keleş Ö, Anderson EH, Huynh J, Gelb J, Freund J, Karakoç A. Stochastic fracture of additively manufactured porous composites. Sci Rep 2018;8(1). https://doi.org/10.1038/s41598-018-33863-4.

[14] Tesarõová M, Heude E, Comai G, Zikmund T, Kaucká M, Adameyko I, et al. An interactive and intuitive visualisation method for X-ray computed tomography data of biological samples in 3D Portable Document Format. Sci Rep 2019;9(1). https://doi.org/10.1038/s41598-019-51180-2.

[15] Vásárhelyi L, Kónya Z, Kukovecz Á, Vajtai R. Microcomputed tomography–based characterization of advanced materials: a review. Mater Today Adv 2020;8:100084. https://doi.org/10.1016/j.mtadv.2020.100084.

[16] Sharma Y, Phillion AB, Martinez DM. Automated segmentation of wood fibres in micro-CT images of paper. J Microsc 2015;260(3):400–10. https://doi.org/10.1111/jmi.12308.

[17] Allahkarami M, Bandla S, Winarski RP, Hanan JC. X-ray nanotomography of a nanofiber: Quantitative measurement of diameter fluctuations. Appl Surf Sci 2014;297:9–15. https://doi.org/10.1016/j.apsusc.2013.12.152.

[18] De Boever W, Diaz A, Derluyn H, De Kock T, Van Stappen J, Dewanckele J, et al. Characterization of composition and structure of clay minerals in sandstone with ptychographic X-ray nanotomography. Appl Clay Sci 2015;118:258–64. https://doi.org/10.1016/j.clay.2015.09.020.

[19] Miettinen A, Oikonomidis IV, Bonnin A, Stampanoni M, Murphy R. NRStitcher: Non-rigid stitching of terapixel-scale volumetric images. Bioinformatics 2019. https://doi.org/10.1093/bioinformatics/btz423.

[20] Chaurand P, Liu W, Borschneck D, Levard C, Auffan M, Paul E, et al. Multi-scale X-ray computed tomography to detect and localize metal-based nanomaterials in lung tissues of in vivo exposed mice. Sci Rep 2018;8(1). https://doi.org/10.1038/s41598-018-21862-4.

[21] Nafar Dastgerdi J, Miettinen A, Parkkonen J, Remes H. Multiscale microstructural characterization of particulate-reinforced composite with non-destructive X-ray micro- and nanotomography. Compos Struct 2018;194:292–301. https://doi.org/10.1016/j.compstruct.2018.04.022.

[22] Bernasconi A, Carboni M, Ribani R. On the combined use of Digital Image Correlation and Micro Computed Tomography to measure fibre orientation in short fibre reinforced polymers. Compos Sci Technol 2020;195:108182. https://doi.org/10.1016/j.compscitech.2020.108182.

[23] Aronsson M, Henningsson O, Sävborg Ö. Slice-based digital volume assembly of a small paper sample. Nord Pulp Pap Res J 2002. https://doi.org/10.3183/npprj-2002-17-01-p029-033.

[24] Bache-Wiig J, Henden PC. Individual fiber segmentation of three-dimensional microtomograms of paper and fiber-reinforced composite materials. Norwegian University of Science and Technology; 2005.

[25] Axelsson M. 3D tracking of cellulose fibres in volume images. In: Proc. - Int. Conf. Image Process. ICIP; 2007. https://doi.org/10.1109/ICIP.2007.4380016.

[26] Viguié J, Latil P, Orgéas L, Dumont PJJ, Rolland du Roscoat S, Bloch J-F, et al. Finding fibres and their contacts within 3D images of disordered fibrous media. Compos Sci Technol 2013;89:202–10. https://doi.org/10.1016/j.compscitech.2013.09.023.

[27] Donoser M, Mauthner T, Bischof H, Kritzinger J. A probabilistic approach for tracking fibers. Proc Int Conf Pattern Recognit 2008. https://doi.org/10.1109/icpr.2008.4761560.

[28] Golkhosh F, Sharma Y, Martinez DM, Lee PD, Tsai W, Courtois L, et al. 4D synchrotron tomographic imaging of network and fibre level micromechanics in softwood paper. Materialia 2020;11:100680. https://doi.org/10.1016/j.mtla.2020.100680.

[29] Malmberg F, Lindblad J, Östlund C, Almgren KM, Gamstedt EK. Measurement of fibrefibre contact in three-dimensional images of fibrous materials obtained from X-ray synchrotron microtomography. Nucl Instruments Methods Phys Res Sect A Accel Spectrometers, Detect Assoc Equip 2011;637(1):143–8. https://doi.org/10.1016/j.nima.2011.01.080.

[30] Lindgren E. Development and Verification of Indirect Test Method for Characterisation of Fibre/Matrix Adhesion in Regenerated Cellulose Fibre Based Composite. Luleå University of Technology; 2015.

[31] Maire E, Withers PJ. Quantitative X-ray tomography. Int Mater Rev 2014;59(1):1–43. https://doi.org/10.1179/1743280413Y.0000000023.

[32] Ekman A, Miettinen A, Tallinen T, Timonen J. Contact formation in random networks of elongated objects. Phys Rev Lett 2014;113(26). https://doi.org/10.1103/PhysRevLett.113.268001.

[33] Saha PK, Zhiyun Gao, Alford SK, Sonka M, Hoffman EA. Topomorphologic separation of fused isointensity objects via multiscale opening: Separating arteries and veins in 3-D pulmonary CT. IEEE Trans Med Imaging 2010;29(3):840–51. https://doi.org/10.1109/TMI.2009.2038224.

[34] Fang Q, Boas DA. Tetrahedral mesh generation from volumetric binary and grayscale images. Proc. - 2009 IEEE Int. Symp. Biomed. Imaging From Nano to Macro, ISBI 2009, 2009. doi:10.1109/ISBI.2009.5193259.

[35] Liu A, Joe B. Relationship between tetrahedron shape measures. BIT 1994;34(2):268–87. https://doi.org/10.1007/BF01955874.

[36] Lagarias JC, Reeds JA, Wright MH, Wright PE. Convergence properties of the Nelder-Mead simplex method in low dimensions. SIAM J Optim 1998;9(1):112–47. https://doi.org/10.1137/S1052623496303470.

[37] Fish J. In: Multiscale Methods: Bridging the Scales in Science and Engineering. https://doi.org/10.1093/acprof:oso/9780199233854.001.0001.

[38] Fish J. In: Practical multiscaling. https://doi.org/10.1007/978-94-009-3489-4.

[39] Geers MGD, Kouznetsova VG, Brekelmans WAM. Computational homogenization. CISM Int Cent Mech Sci Courses Lect 2010. https://doi.org/10.1007/978-3-7091-0283-1_7.

[40] Karakoç A, Paltakari J, Taciroglu E. Data-Driven Computational Homogenization Method Based on Euclidean Bipartite Matching. J Eng Mech 2020;146(2):04019132. https://doi.org/10.1061/(ASCE)EM.1943-7889.0001708.

[41] Karakoç A, Paltakari J, Taciroglu E. On the computational homogenization of three-dimensional fibrous materials. Compos Struct 2020;242:112151. https://doi.org/10.1016/j.compstruct.2020.112151.

[42] Karakoç A, Taciroglu E. Optimal automated path planning for infinitesimal and real-sized particle assemblies. AIMS Mater Sci 2017. https://doi.org/10.3934/matersci.2017.4.847.

[43] Rendl F. On the Euclidean assignment problem. J Comput Appl Math 1988;23(3):257–65. https://doi.org/10.1016/0377-0427(88)90001-5.

[44] Cordenka GMBH. Cordenka 700 Super 3 Data Sheet 2020.

[45] NatureWorks. Ingeo Biopolymer 2003D Technical Data Sheet 2020:4.

[46] ASTM-D638-14. Standard Test Method for Tensile Properties of Plastics. ASTM Stand 2014.

[47] Banterle F, Corsini M, Cignoni P, Scopigno R. A low-memory, straightforward and fast bilateral filter through subsampling in spatial domain. Comput Graph Forum 2012. https://doi.org/10.1111/j.1467-8659.2011.02078.x.

[48] Otsu N. Threshold selection method from gray-level histograms. IEEE Trans Syst Man Cybern 1979. https://doi.org/10.1109/tsmc.1979.4310076.

[49] Jähne B. Practical handbook on image processing for scientific and technical applications, second edition. 2004.

[50] Gindl W, Reifferscheid M, Adusumalli R-B, Weber H, Röder T, Sixta H, et al. Anisotropy of the modulus of elasticity in regenerated cellulose fibres related to molecular orientation. Polymer (Guildf) 2008;49(3):792–9. https://doi.org/10.1016/j.polymer.2007.12.016.

[51] Northolt MG, Boerstoel H, Maatman H, Huisman R, Veurink J, Elzerman H. The structure and properties of cellulose fibres spun from an anisotropic phosphoric acid solution. Polymer (Guildf) 2001. https://doi.org/10.1016/S0032-3861(01)00211-7.

[52] Sedighi-Gilani M, Navi P. Experimental observations and micromechanical modeling of successive-damaging phenomenon in wood cells' tensile behavior. Wood Sci Technol 2007;41(1):69–85. https://doi.org/10.1007/s00226-006-0094-5.

[53] Wolfram Research Inc. Mathematica 12.0. Wolfram Res 2019.

[54] Maccone C. A simple introduction to the KLT (Karhunen—Loève Transform). Deep Sp.. Flight Commun 2009. https://doi.org/10.1007/978-3-540-72943-3_10.

[55] Rodríguez-Cantano R, Sundnes J, Rognes ME. Uncertainty in cardiac myofiber orientation and stiffnesses dominate the variability of left ventricle deformation response. Int j Numer Method Biomed Eng 2019;35(5):e3178. https://doi.org/10.1002/cnm.v35.510.1002/cnm.3178.